The electronic structure of the primary electron donor of reaction centers of purple bacteria at atomic resolution as observed by photo-CIDNP C-13 NMR

Daviso, E.; Prakash, S.; Alia, A.; Gast, P.; Neugebauer, J.; Jeschke, G.; Matysik, J.

The electronic structure of the primary electron donor of reaction centers of purple bacteria at atomic resolution as observed by photo-CIDNP ^{13}C NMR

Eugenio Daviso[a], Shipra Prakash[a], A. Alia[a], Peter Gast[b], Johannes Neugebauer[a], Gunnar Jeschke[c], and Jörg Matysik[a,1]

[a]Leiden Institute of Chemistry, 2300 RA Leiden, The Netherlands; [b]Leiden Institute of Physics, 2300 RA Leiden, The Netherlands; and [c]Laboratorium für Physikalische Chemie, Eidgenössische Technische Hochschule Zürich, 8093 Zürich, Switzerland

Edited by Steven G. Boxer, Stanford University, Stanford, CA, and approved October 23, 2009 (received for review July 30, 2009)

Composed of the two bacteriochlorophyll cofactors, P_L and P_M, the special pair functions as the primary electron donor in bacterial reaction centers of purple bacteria of *Rhodobacter sphaeroides*. Under light absorption, an electron is transferred to a bacteriopheophytin and a radical pair is produced. The occurrence of the radical pair is linked to the production of enhanced nuclear polarization called photochemically induced dynamic nuclear polarization (photo-CIDNP). This effect can be used to study the electronic structure of the special pair at atomic resolution by detection of the strongly enhanced nuclear polarization with laser-flash photo-CIDNP magic-angle spinning NMR on the carotenoid-less mutant R26. In the electronic ground state, P_L is strongly disturbed, carrying a slightly negative charge. In the radical cation state, the ratio of total electron spin densities between P_L and P_M is 2:1, although it is 2.5:1 for the pyrrole carbons, 2.2:1 for all porphyrinic carbons, and 4:1 for the pyrrole nitrogen. It is shown that the symmetry break between the electronic structures in the electronic ground state and in the radical cation state is an intrinsic property of the special pair supermolecule, which is particularly attributable to a modification of the structure of P_L. The significant difference in electron density distribution between the ground and radical cation states is explained by an electric polarization effect of the nearby histidine.

electron transfer | nuclear polarization | photosynthesis | solid-state NMR | electronic structure

The essential steps in photosynthesis, photon absorption, and electron transfer occur in the reaction center (RC) membrane protein. Simple purple photosynthetic bacteria possess only a single type of RC and perform anoxygenic photosynthesis. In RCs from the purple bacterium *Rhodobacter sphaeroides* R26, the primary electron donor (P), called the special pair, consists of two symmetrically arranged BChl *a* (Fig. 1*A*) cofactors, labeled P_L and P_M, coordinated by His-L168 and His-M202, respectively (Fig. 1*B*) (1, 2). The other cofactors are two accessory BChls, two BPhes *a*, two ubiquinones, and a nonheme iron that are arranged in a nearly C_2 symmetry. Despite the symmetrical arrangement, the electron pathway is entirely unidirectional, occurring along the L branch (for review, see ref. 3).

In the dark electronic ground state, the symmetry between both cofactors P_L and P_M is already broken, as was shown with photochemically induced dynamic nuclear polarization (photo-CIDNP) ^{13}C magic-angle spinning (MAS) NMR (4). The ratio of electron spin densities between the two cofactors in the radical cation state has been determined at the molecular level to be ≈2:1 using ^{1}H electron nuclear double resonance (ENDOR) (5, 6) and steady-state photo-CIDNP ^{13}C MAS NMR (7). On the other hand, values of ≈5:1 have been observed by ^{15}N-ESEEM (ESEEM, electron spin echo envelope modulation) (8) and values of ≈4:1 have been observed by time-resolved photo-CIDNP ^{15}N MAS NMR (9). It has been proposed that this difference is caused by distinct conformations of the RC (8) or by the different positions of the nuclei observed (9). As measured from the CH_3 hyperfine couplings at positions 2^1 and 12^1 by ^{1}H ENDOR, mutant RCs (10, 11) have ratios of electron spin densities between ≈5:1 and ≈1:5. Detergents have also been shown to redistribute electron spin densities significantly (12).

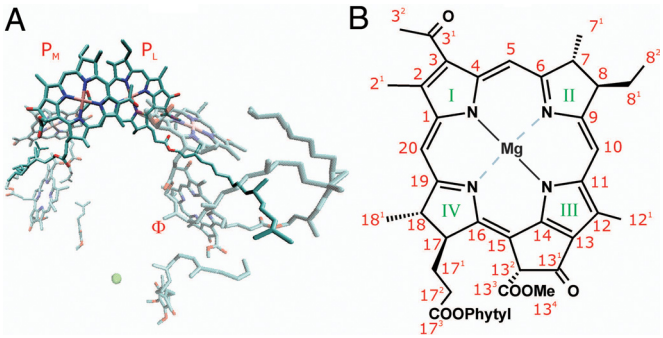

Fig. 1. (*A*) Arrangement of cofactors in the RC of *Rb. sphaeroides* R26 (PDB ID code 1AIJ). The two BChl cofactors forming the special pair are labeled as P_L and P_M. The primary electron acceptor is labeled as Φ. For the sake of clarity, protein chains are omitted. (*B*) BChl*a* molecule with numbering of carbon atoms according to the International Union of Pure and Applied Chemistry (IUPAC) nomenclature.

To understand the origin of this experimentally observed variation in electron spin density distribution, the present work aims to zoom into the electronic structure of the special pair from the molecular resolution to the atomic resolution. To that end, photo-CIDNP, which occurs in frozen and quinone-removed RCs, was studied by MAS NMR. The origin of the solid-state photo-CIDNP effect in frozen and quinone-blocked RCs of *Rb. sphaeroides* R26 at high magnetic fields (13–16) is now understood (17); for reviews, see the publications by Matysik and Jeschke (14) and Daviso et al. (18).

A single photocycle is presented in Fig. 2. From the photochemically excited P*, an electron is transferred to the primary acceptor, Φ. This light-induced spin-correlated radical pair is created in a nonstationary and highly electron polarized singlet state. The radical pair undergoes two processes:

(*i*) Intersystem crossing (ISC) driven by the isotropic hyperfine iteration a_{iso} and the difference in *g* values of the electrons leads to a coherent oscillation between the singlet (S) and the triplet

Author contributions: J.M. designed research; E.D. performed research; E.D., S.P., A.A., and P.G. contributed new reagents/analytic tools; E.D., J.N., G.J., and J.M. analyzed data; and E.D., J.N., G.J., and J.M. wrote the paper.

The authors declare no conflict of interest.

This article is a PNAS Direct Submission.

Data deposition: The atomic coordinates and structure factors have been deposited in the Protein Data Bank, www.pdb.org (PDB ID code 1AIJ).

[1]To whom correspondence should be addressed. E-mail: j.matysik@chem.leidenuniv.nl.

This article contains supporting information online at www.pnas.org/cgi/content/full/0908608106/DCSupplemental.

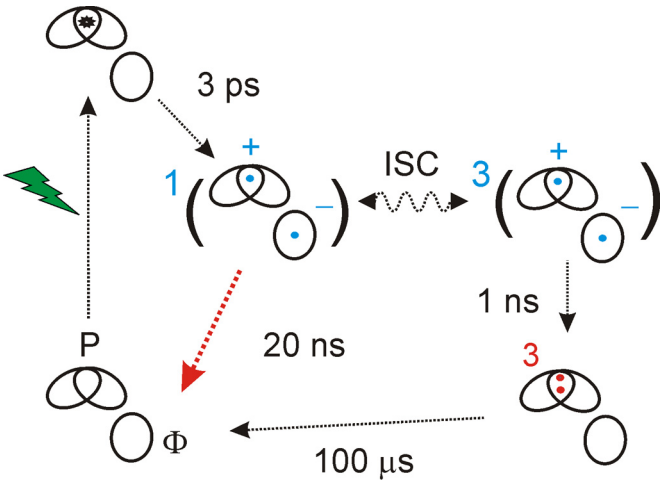

Fig. 2. Kinetics and spin dynamics of electron transport in quinone-depleted RCs of *Rb. sphaeroides* R26. After absorption of a photon from the photochemically excited singlet state of the primary donor P*, an electron is transferred to the primary acceptor Φ, a BPhe cofactor. This initial singlet radical pair $^1(P^{+}\Phi^{-})$ is in a nonstationary state and is highly electron-polarized. An electron back-transfer leads to the electronic ground state (red dashed arrow). Because of the difference in *g* values and hfi, the singlet radical pair evolves into a triplet radical pair $^3(P^{+}\Phi^{-})$, whereas the influence of hfi leads to spin-sorting between singlet and triplet pairs. Concomitantly to this process of ISC, electron polarization is transferred to nuclei by the TSM and DD mechanisms. Net nuclear polarization is created by unbalancing the decay pathways of the singlet and the triplet radical pair (singlet and triplet branches). The differential relaxation occurs on signals of the donor, because nuclear spin relaxation is significant during the lifetime of the ^{3}P. In time-resolved experiments, TNP from the singlet decay channel can be observed directly, because the nuclear polarization of the triplet decay pathway (triplet branch, dotted arrow) reaches the ground state with a delay of 100 μs.

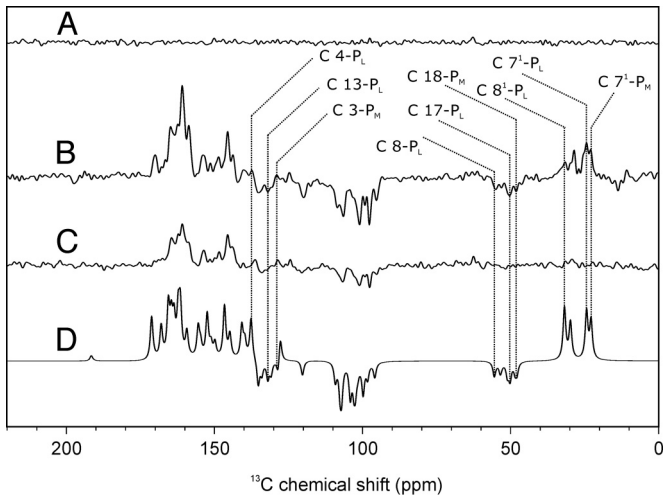

Fig. 3. ^{13}C Photo-CIDNP MAS NMR spectra of natural abundance RCs of *Rb. sphaeroides* R26 obtained in the dark (*A*), immediately after the nanosecond flash (*B*), and 400 μs after the light flash (*C*) using 532-nm 8-ns flashes. The intensities of *B* are proportional to the isotropic hfi. All the spectra have been collected at a magnetic field of 4.7 T and a temperature of −40 ° Celsius. *D* shows the simulated TNP occurring in the S and projected out in the diamagnetic ground state.

(T_0) states of the radical pair. The S state enriches the α-nuclear spin state (with ^{13}C having a positive gyromagnetic ratio), whereas the T_0 state enriches β-nuclear spins. Therefore, nuclear spin populations oscillating between α- and β-spin states during ISC lead to transient nuclear polarization (TNP). In addition, the evolution of the spin system leads to three-spin mixing (TSM), which transfers the electron polarization to nuclei on the nanosecond time scale by mixing electronic and nuclear states under the action of the anisotropic hyperfine interaction (ΔA) and the electron–electron dipolar coupling d′ (see *SI*) (19).

(*ii*) Electron back-transfer to the special pair can occur in the S and T_0 states having different lifetimes of the two decay channels (Fig. 2). This kinetic symmetry breaking, together with ΔA, creates additional nuclear polarization by the differential decay (DD) mechanism (20).

Both the TSM and DD contribute to the photo-CIDNP build-up by unbalancing the ratio of α- to β-nuclear spins in the two decay channels. Both mechanisms require ΔA and have been shown to explain the results of steady-state photo-CIDNP MAS NMR experiments under continuous illumination (7). According to theoretical considerations (21) and numerical simulations (17), the polarization arising at the end of the photocycle in *Rb. sphaeroides* WT from these two mechanisms is roughly proportional to ΔA^2, and thus to the square of *p* spin density on the carbon atoms.

Under the steady-state conditions achieved with continuous illumination, excited states are not significantly populated; hence, the TNP caused by the a_{iso} is not observed, because the contributions have opposite signs and the same magnitude in the two decay channels, and thus cancel on return to the ground state. Therefore, the radical pair mechanism (RPM) (22, 23), which is known from liquid photo-CIDNP NMR, cannot contribute to solid-state photo-CIDNP under continuous illumination. On the other hand, because of development of time-resolved photo-CIDNP MAS NMR (24), the TNP can be observed selectively from the electronic S state (9, 17). In such experiments, the light pulse for excitation (≈8 ns) and the NMR pulse for detection (≈4 μs) are much shorter than the lifetime of the P molecular triplet state (^{3}P) state of R26 RCs (≈100 μs) (Fig. 2). Thus, TNP of the S state can be transiently detected on an electronic ground state population that arises primarily from the singlet decay pathway, whereas nuclear spins in the triplet branch are still invisible because of paramagnetic broadening (17). Thus, effects attributable to isotropic coupling between electrons and nuclei become observable, similar to RPM-based photo-CIDNP in liquids. The sign rules are the same as for cage products from a singlet-born pair in RPM-based photo-CIDNP (25). Therefore, the time-resolved experiment can provide estimates of the a_{iso} (*vide infra*).

In this work, the experimentally directly accessible TNP intensities are used to reconstruct the electronic structure of the special pair in its radical cation state at atomic resolution. The strong signal enhancement allows for assignment of the associated ^{13}C chemical shifts (CSs) and subsequent reconstruction of the ground state electronic structure.

Results

Time-Resolved ^{13}C Photo-CIDNP MAS NMR. Fig. 3 shows the ^{13}C MAS NMR spectra of RCs of *Rb. sphaeroides* R26 collected in the dark (spectrum 3A) and in a time-resolved experiment in which light excitation was followed by an NMR detection pulse of 4 μs with a delay of 0 μs, with this being a time scale much shorter than the triplet donor lifetime (spectrum 3B) and that of 400 μs (spectrum 3C). Spectrum 3A shows no signal, demonstrating that all signals in spectra 3B and 3C are light-induced. Spectrum 3B presents the TNP occurring in the ground state from the singlet decay branch only. Spectrum 3C, representing the full photo-CIDNP build-up after one photocycle, agrees within the noise level of the spectrum obtained in the steady state under continuous illumination (26). Spectra 3B and 3C are distinguished, for example, in the aliphatic region (between 0 and 55 ppm), where positive (20–35 ppm) and negative (45–55

ppm) signals appear only transiently, and in the aromatic region, where a transient negative feature at 120–135 ppm emerges.

CS Assignments by ^{13}C photo-CIDNP MAS NMR. Spectrum 3B has been analyzed with fitting Lorentzians (Fig. S1). These fits were based on ^{13}C chemical shift (CS) assignments of the P obtained in previous studies (4, 7, 26, 27) (Tables S1 and S2). For reconstruction of the ground state electronic structure, the empirically obtained CSs have been corrected for ring-current-induced shifts (Tables S1 and S2). Based on these assignments, maps at atomic resolution can be constructed from the experimentally obtained local electron densities of the electronic ground state (Fig. 4 *A* and *A′*) as well as from the experimentally obtained local electron spin densities of the radical cation state (Fig. 4 *B* and *B′*).

Simulation of TNP Intensities. Based on the x-ray structure of the R26-RC by Stowell et al. (28), the isotropic hyperfine interaction (hfi) values of the a_{iso} have also been obtained from *s* spin densities on the carbon atoms of the radical cation of the P by density functional theory (DFT) calculations (Figs. S2 and S3, Tables S5 and S6). Based on the theory, TNP intensities have been computed, and with the CS assignments, spectrum 3D has been simulated assuming that the photo-CIDNP intensities are proportional to the a_{iso}. The general good agreement between experiment and simulation supports the theoretical prediction (see *SI Materials and Methods*) that the polarization arising from the S state is indeed proportional to the a_{iso}. Further support is obtained by simulating coupled-spin dynamics and decay kinetics of the radical pair with a density matrix approach and correlating the computed TNP polarizations originating from singlet pairs with the a_{iso} values used in the input spin Hamiltonian. We find linear correlation with a correlation coefficient of 0.8779. Hence, to a good approximation, ratios of intensities of the spectral lines in the photo-CIDNP spectrum obtained at a delay time of 0 μs with a 4-μs NMR detection pulse are proportional to ratios of the corresponding a_{iso}s (Fig. 3*B*, Tables S1 and S2). Except for effects of electron–electron correlation in the wave function, a_{iso}, in turn, is proportional to the *s* spin density of the nucleus under consideration, which is obtained by representing the wave function as a linear combination of atomic orbitals. Relative spectral line intensities can thus be used to reconstruct a map of the electron spin density distribution of the special pair (Fig. 4 *C* and *C′*).

Discussion

Electron Density Aberrations in the Ground State of the P. The influence of interactions between the two chromophores and of the scaffolding protein on the electron density distribution in the electronic ground state of the special pair can be estimated from the difference in the ^{13}C CSs between photo-CIDNP MAS NMR data of the special pair and NMR data of a BChl molecule in solution in acetone (29, 30). In Fig. 4 *A* and *A′*, the yellow spheres represent up-field shifts, which are caused by an increase of local electron density, whereas the orange spheres represent down-field shifts (see *SI Materials and Methods*). The prevalence of up-field shifts indicates that the total electron density in the ground state is increased compared with that of a BChl molecule in acetone solution, suggesting that the special pair carries a partial negative charge induced by the protein, presumably via hydrogen-bonding interactions via the His-L173 coordinated with the oxygen of the C-3′ acetyl of P_L. The electron density is significantly increased in the overlapping region of the cofactors formed by the two pyrrole rings I, particularly on cofactor P_L. This distribution enhances interaction between the two moieties of the special pair, thus lowering excitation energy and making this pair a better energy sink for excitation transfer from light-harvesting pigments.

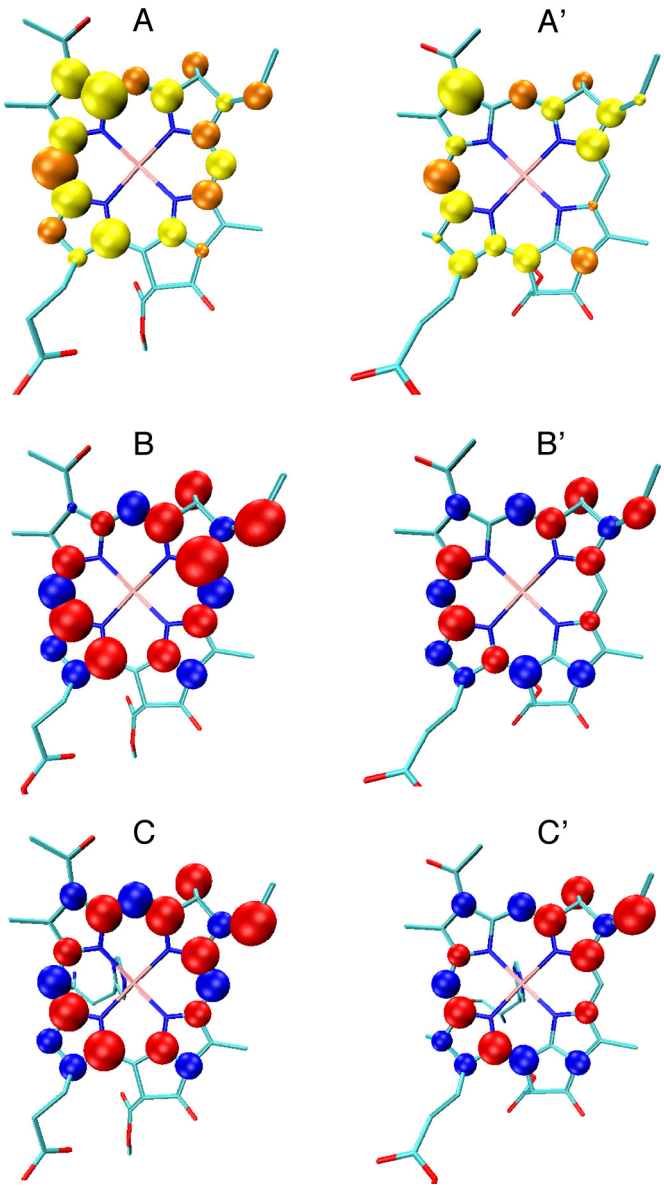

Fig. 4. Electronic structures of the P. The chlorophylls depicted have the same orientation as in Fig. 1*B*, which can be consulted for the labeling of the pyrrole rings. (*A* and *A′*) Relative electron densities of P_L and P_M in the electronic ground state derived from CS differences with respect to monomeric chlorophyll in acetone considering ring-current effects. (*B* and *B′*) ^{13}C electron spin densities on P_L and P_M obtained experimentally from TNP intensities observed at zero delay between light excitation and NMR detection. (*C* and *C′*) Normalized local isotropic hfi values with the a_{iso}s of ^{13}C in P_L and P_M derived from DFT computations considering P_L and P_M coordinated to His-L173 and His-M202, respectively. To compare the experimental data with theory, both datasets were normalized by setting the cumulative volume of the red and blue spheres to a fixed value for optimal visualization (see *SI Materials and Methods*).

The CSs are significantly different between the two parts of the special pair (Tables S1 and S2), as proposed earlier by Schulten et al. (4). The concentration of electron density of pyrrole ring I of cofactor P_L is linked to up-field shifts of up to 14 ppm, which cannot be explained by ring-current shifts (Tables S1 and S2). The high electron density of both pyrrole rings I may be stabilized by the hydrogen bond interaction between the protein and the special BChl *a* of the special pair. The existence of this hydrogen bond (31–33) and its crucial role for the

electronic structure have been proposed earlier (11, 34). On the other hand, several significant down-field shifts in a range of 7–10 ppm occur, especially at the C-5 and C-20 methine carbons of both P_L and P_M. Hence, the strong increase of electron density on pyrrole ring I of P_L is partially attributable to a local redistribution of charge. The origin of this effect may be the formation of a supramolecular electronic structure.

Previous resonance Raman (35) and steady-state ^{13}C photo-CIDNP MAS experiments (4) suggest that one of the BChl cofactors is peculiar within the special pair in the electronic ground state. Here, we show that P_L is the special BChl cofactor among the four.

Electron Spin Densities in the Radical Cation State. Fig. 4 *B* and *B′* show the map of ^{13}C photo-CIDNP intensities of P_L and P_M in the radical cation state obtained from the spectrum collected by a light pulse followed by an NMR detection pulse much shorter than the lifetime of the triplet ^3P (*vide infra*).

The size of the spheres is proportional to the magnitude of the a_{iso}. The red spheres represent positive (absorptive) NMR signals associated with an excess of α-nuclear spin states, whereas the blue spheres are associated with negative (emissive) signals attributable to excess of β-nuclear spin states. According to RPM sign rules that also apply to TNP, absorptive and emissive signals are associated with positive and negative a_{iso}s, respectively. The size of the spheres has been normalized on the most intense signal arising from C-9 of P_L (161 ppm). The ratio of the total electron spin densities in *s* orbitals on the detected carbon atoms between both cofactors is (68 ± 4):(32 ± 4) in favor of P_L (Tables S1 and S2). Hence, the molecular electron spin density distribution is in very good agreement with previous ^1H ENDOR studies (6), which inferred carbon spin densities from the a_{iso}s of directly bonded protons via McConnell relations, and with steady-state ^{13}C-photo-CIDNP studies (7), which are sensitive to the spin densities in the carbon $2p_z$ orbitals that dominate the anisotropic contribution to the ^{13}C hyperfine coupling.

Zooming into the atomic scale, the electron spin density is localized mainly on the periphery of the special pair, whereas the central overlapping region appears to be emptied. It seems that the supramolecular structure now stabilizes the electron hole.

In addition to the supramolecular asymmetry (P_L over P_M) and the molecular asymmetry (pyrrole rings II and IV over rings I and III), a symmetry break occurs on the level of the pyrrole rings. Particularly high electron spin density is observed on the carbons of pyrrole rings II (20%) and IV (20%) of P_L. Interestingly, this is mainly in favor of the direction toward the primary acceptor. The electron spin density distribution of the carbons of the porphyrin system is 5:2 in favor of P_L. Considering the electron spin densities residing on the eight nitrogens, a ratio of 4:1 in favor of P_L occurs (see *SI Materials and Methods*). This is in very good agreement with ^{15}N ENDOR (8) and ^{15}N time-resolved photo-CIDNP MAS NMR data (9). Therefore, the asymmetry of the supramolecular electronic structure of the special pair in the radical cation state is more pronounced in the core region than in the periphery. Hence, the symmetry is broken in more than one respect, as demonstrated in Fig. S4.

Fig. 4 *C* and *C′* presents the map of normalized a_{iso}s, which have been obtained by DFT calculations (see *SI Materials and Methods*) considering P_L and P_M separately as well as their axial histidine ligands. Side-chain conformations of the macrocycles, as observed in the crystal structure, have been taken into account. The results of our calculations are in good agreement with recent independent DFT calculations by Yamasaki et al. (36) employing hybrid functionals with varying amounts of exact exchange. In particular, the phase patterns of electron spin density distribution agree despite the fact that Yamasaki et al. (36) display the pattern of local total electron spin densities, whereas we show the local isotropic a_{iso}s, which correlate with the electron spin density in the *s* orbitals. Both calculations also suggest an electron spin density distribution between P_L and P_M of about 60:40.

The alternating phase pattern found by the calculations (Fig. 4 *C* and *C′*) exactly matches the one observed spectroscopically (Fig. 4 *B* and *B′*). In addition, the electron spin density ratio between P_L and P_M is in good agreement between theory and experiment. The successful theoretical simulation implies that the asymmetry in the radical cation is an intrinsic property of the special pair complex with its axial histidines and is caused by geometrical differences conserved by the matrix. Hence, the matrix effect is predominantly attributable to local conformational conservation and caused neither by a far-reaching Coulomb interaction of charged amino acids nor by overlap with other cofactors or aromatic amino acids. In other words, the protein matrix induces the asymmetry by imposing special chlorophyll geometries rather than by delocalization of the wave function beyond the chlorophylls. Interestingly, the matrix has been shown to be extremely rigid and without structural heterogeneities (37, 38). As already assumed by Diller et al. (39) on the basis of photo-CIDNP MAS NMR on photosystem II, cofactor–matrix units of functional relevance are conserved in evolution. That principle may explain the observation by Shelnutt et al. (40) on porphins that cofactor geometries are related to their function.

The maximum close to the primary acceptor may be related to locally enhanced orbital coefficients facilitating electron transfer into the L branch. It appears that the special properties of P_L, which are well reflected in the calculations, are an inherent function of the special pair supermolecule.

Comparison of Electronic Structures in Ground and Radical Cation States. The local electron density of the special pair in its electronic ground state has the maximum in the inner part of the supramolecule, in the overlapping region of the two pyrrole rings I, whereas the electron spin density map of the radical pair state shows a clear and significant asymmetry toward the primary electron acceptor in the active branch. Remarkably, both maxima are found in the special BChl cofactor (P_L).

Both electronic structures elucidated, that of the electronic ground state as well as that of the radical cation state, reflect the same molecular orbital that is the HOMO of the special pair. However, within the static model of the Marcus theory, the differences between the two electronic structures are unexpected. Therefore, the significant differences must reflect the effects of the surrounding of the highest occupied molecular orbital (HOMO). Hence, we conclude that the matrix undergoes local electric polarization effects. Such an local electric polarization effect of the matrix is consistent with and lends support to the previous assumption that the hydrogen bond between the C-3^1 acetyl of P_L and His-L173 stabilizes the charge in the central overlapping region of the special pair in its electronic ground state, although it is broken or weakened in the radical cation state (11, 34). This, in turn, may locally change the dielectric constant of the protein matrix and may help to prevent the back-electron transfer.

Materials and Methods

Sample Preparation. The RCs from *Rb. sphaeroides* R26 were isolated by the procedure of Feher and Okamura (41). The removal of the quinones has been done by incubating the RCs at a concentration of 0.6 μM in 4% (vol/vol) lauryldimethylamine-oxide (LDAO), 10 mM *o*-phenanthroline, 10 mM Tris buffer, pH 8.0, for 6 h at 26 °C, followed by washing with 0.5 M NaCl in 10 mM Tris buffer, pH 8.0, containing 0.025% LDAO and 1 mM EDTA (42). Double-approximately 5 mg of the RC protein complex embedded in LDAO micelles was used for NMR measurements.

MAS NMR Experiments. NMR experiments were performed with an Avance-200 NMR spectrometer equipped with a MAS probe (Bruker). The sample was loaded into a clear 4-mm sapphire rotor and inserted into the MAS probe, and it was frozen slowly at a low-spinning frequency of 800 Hz to ensure a homogeneous sample distribution against the rotor wall (37). The light and dark spectra were collected with a spin-echo pulse sequence with the cyclically ordered phase sequence (CYCLOPS) phase cycle of the (π/2) pulse and detection under two pulse-phase modulation carbon-proton decoupling (43) at a temperature of -40 ° Celsius. The optimum length of the (π/2) carbon pulse, determined on uniformly ^{13}C-labeled tyrosine, was $\approx$4 μs under our experimental conditions using a rf power of $\approx$250 W.

A pulsed nanosecond flash laser provides sufficient radiation intensity for time-resolved photo-CIDNP MAS NMR studies and does not decrease the time resolution that can be obtained in NMR experiments.

The laser was operated with repetition rates between 1 and 4 Hz. Using 1,064-nm flashes of a neodynium yttrium-aluminium garnet (Nd:YAG) laser (Quanta-Ray INDI 40–10; SpectraPhysics), on frequency-doubling with a second harmonic generator, 532-nm laser flashes with pulse lengths of 6–8 ns and energy between 20 and 150 mJ were produced.

Time-resolved photo-CIDNP MAS NMR data were acquired using a presaturation pulse sequence to erase polarization and coherence from previous scans as described by Daviso et al. (24). The delay times between light excitation and NMR detection used were 0 and 400 μs. The rotational frequency for MAS was 8 kHz in all experiments. A cycle delay of 133 ms was used. All the ^{13}C MAS NMR spectra were referenced to the ^{13}COOH response of solid tyrosine·HCl at 172.1 ppm.

Spectral Fitting. The fitting of the spectrum collected using time-resolved MAS NMR photo-CIDNP of pure RCs of *Rb. sphaeroides* R26 has been performed using Igor Pro 6.01. The peaks are Lorentzian with a full width at half height (FWHH) between 40 and 60 Hz as experimentally observed using the 4-ALA labeling pattern of *Rb. sphaeroides* WT (24) (WaveMetrics). A typical characteristic fitting result is shown in Fig. S1.

DFT Calculations of the Radical Cation of the P. DFT computations of hyperfine coupling tensors were performed with the Amsterdam density functional program (ADF) 2002.1 package (SCM NV), using the triple-Zeta basis set with polarization functions on all atoms (TZP) all-electron basis set for all atoms as described (17, 26). Geometries of ground state molecules were taken from the crystal structure in the charge-neutral state [Protein Data Bank (PDB) ID code 1AIJ] (28) and subjected to geometry optimization within ADF in the cation radical state. Details are given in *SI Materials and Methods*.

Numerical Simulations of TNP Intensities. Numerical simulations start from a pure S and compute the time evolution under a Hamiltonian, including electron Zeeman, nuclear Zeeman, and hfi as well as dipole–dipole and exchange coupling between the two electron spins. The part of the density matrix that decays to the ground state from either the S or T_0 state is projected out (diamagnetic part) and is further evolved under a Hamiltonian, including only the nuclear Zeeman interaction. Details are given in *SI Materials and Methods*.

Calculations of Ring-Current Shifts. To estimate ring-current shifts, we calculated nucleus-independent CSs (44) at the positions of the nuclei of monomer P_M in a calculation on monomer P_L, or vice versa, with the NMR module (45) of the ADF program (46, 47). These shifts were obtained with the Becke-Perdew exchange-correlation functional (BP86) (48, 49) and a TZP basis set from the ADF basis set library (46). Tests with a very large basis of quadruple-Zeta quality with four sets of polarization functions resulted in small changes (typically smaller than 0.1 ppm) of the shifts. The structure of the special pair used in the calculations was derived from the crystal structure with PDB ID code 1AIJ (28). The dimer of BChl molecules, the axial histidine ligands, and the histidine ligand coordinated to the acetyl group at the C-3 position of P_L were extracted from that structure. Hydrogen atoms were added, and their positions were relaxed in a BP86/TZP calculation employing an empirical dispersion correction (50). The phytyl chains of the BChl molecules were replaced by methyl groups. All histidine ligands were assumed to be neutral.

ACKNOWLEDGMENTS. The help of F. Lefeber, K. B. Sai Sankar Gupta, and K. Erkelens is gratefully acknowledged. The authors thank Dr. B. Bode for exciting discussions. J.M. thanks Prof. H. J. M. de Groot for continuous support. This work has been financially supported by the Netherlands Organization for Scientific Research (NWO) through Jonge Chemici Award (700.50.521), an open-competition grant (700.50.004), and a Vidi grant (700.53.423), as well as the Volkswagen-Stiftung (I/78010, to J.M.). E.D. thanks EMBO for a short-term fellowship (ASTF-131-2005).

1. Komiya H, et al. (1988) Structure of the reaction center from *Rhodobacter-sphaeroides* R-26 and 2.4.1. *Proc Natl Acad Sci USA* 85:9012–9016.
2. Camara-Artigas A, Brune D, Allen JP (2002) Interactions between lipids and bacterial reaction centers determined by protein crystallography. *Proc Natl Acad Sci USA* 99:11055–11060.
3. Hoff AJ, Deisenhofer J (1997) Photophysics of photosynthesis. Structure and spectroscopy of reaction centers of purple bacteria. *Phys Rep* 287:2–247.
4. Schulten EAM, et al. (2002) C-13 MAS NMR and photo-CIDNP reveal a pronounced asymmetry in the electronic ground state of the special pair of *Rhodobacter sphaeroides* reaction centers. *Biochemistry* 41:8708–8717.
5. Huber M (1997) On the electronic structure of the primary electron donor in bacterial photosynthesis. *Photosynth Res* 52:1–26.
6. Lendzian F, et al. (1993) The electronic structure of the primary donor cation-radical in *Rhodobacter sphaeroides* R26. *Biochim Biophys Acta* 1183:139–160.
7. Prakash S, et al. (2005) Magnetic field dependence of photo-CIDNP MAS NMR on photosynthetic reaction centers of *Rhodobacter sphaeroides* WT. *J Am Chem Soc* 127:14290–14298.
8. Käss H, et al. (1995) 2D ESEEM of the N-15-labeled radical cations of bacteriochlorophyll *a* and of the primary donor in reaction centers of *Rhodobacter-sphaeroides. J Phys Chem* 99:436–448.
9. Daviso E, et al. (2009) Nanosecond-flash ^{15}N photo-CIDNP MAS NMR on reaction centers of *Rhodobacter sphaeroides* R26. *Org Magn Res*, in press.
10. Artz K, et al. (1997) Relationship between the oxidation potential and electron spin density of the primary electron donor in reaction centers from *Rhodobacter sphaeroides. Proc Natl Acad Sci USA* 94:13582–13587.
11. Rautter J, et al. (1995) ENDOR studies of the primary donor cation-radical in mutant reaction centers of *Rhodobacter sphaeroides. Biochemistry* 34:8130–8143.
12. Müh F, Rautter J, Lubitz W (1997) Two distinct conformations of the primary electron donor in reaction centers from *Rhodobacter sphaeroides. Biochemistry* 36:4155–4162.
13. Daviso E, et al. (2008) in *Energy from the Sun*, eds Allen J, Gantt E, Golbeck J, Osmond B (Springer, Dordrecht), pp 63–66.
14. Matysik J, Jeschke G (2003) A reassessment of the origin of photochemically induced dynamic nuclear polarization effects in solids. *Chem Phys* 294:239–255.
15. Zysmilich MG, McDermott A (1994) Photochemically induced dynamic nuclear-polarization in the solid-state N-15 spectra of reaction centers from photosynthetic bacteria. *J Am Chem Soc* 116:8362–8363.
16. Zysmilich MG, McDermott A (1996) Natural abundance solid-state carbon NMR studies of photosynthetic reaction centers with photoinduced polarization. *Proc Natl Acad Sci USA* 93:6857–6860.
17. Daviso E, et al. (2009) Electron-nuclear spin dynamics in a bacterial photosynthetic reaction center. *J Phys Chem C* 113:10269–10278.
18. Daviso E, Jeschke G, Matysik J (2008) in *Biophysical Techniques in Photosynthesis*, eds Aartsma T, Matysik J (Springer, Dordrecht), Vol II, pp 385–399.
19. Jeschke G (1997) Electron-electron-nuclear three-spin mixing in spin-correlated radical pairs. *J Chem Phys* 106:10072–10086.
20. Polenova T, McDermott AE (1999) A coherent mixing mechanism explains the photo-induced nuclear polarization in photosynthetic reaction centers. *J Phys Chem B* 103:535–548.
21. Diller A, et al. (2007) Signals in solid-state photochemically induced dynamic nuclear polarization recover faster than signals obtained with the longitudinal relaxation time. *J Phys Chem B* 111:10606–10614.
22. Closs GL, Closs LE (1969) Induced dynamic nuclear spin polarization in reactions of triplet diphenylmethylene. *J Am Chem Soc* 91:4549–4550.
23. Kaptein R, Oosterhoff JL (1969) Chemically induced dynamic nuclear polarization II: Relation with anomalous ESR spectra. *Chem Phys Lett* 4:195–197.
24. Daviso E, et al. (2008) Photo-CIDNP MAS NMR beyond the T_1 limit by fast cycles of polarization extinction and polarization generation. *J Magn Reson* 190:43–51.
25. Kaptein R (1971) Simple rules for chemically induced dynamic nuclear polarization. *Chem Comm* 732–733.
26. Prakash S, et al. (2006) Photo-CIDNP MAS NMR in intact cells of *Rhodobacter sphaeroides* R26. *J Am Chem Soc* 128:12794–12799.
27. Prakash S, et al. (2007) C-13 chemical shift map of the active cofactors in photosynthetic reaction centers of *Rhodobacter sphaeroides* revealed by photo-CIDNP MAS NMR. *Biochemistry* 46:8953–8960.
28. Stowell MHB, et al. (1997) Light-induced structural changes in photosynthetic reaction center. *Science* 276:812–816.
29. Abraham RJ, Rowan AE (1991) in *Chlorophylls*, ed Scheer H (CRC, Boca Raton), pp 797–834.
30. Prakash S (2006) PhD Thesis (Universiteit Leiden).
31. Ermler U, Fritzsch G, Buchanan SK, Michel H (1994) Structure of the photosynthetic reaction center from *Rhodobacter sphaeroides. Structure* 2:925–936.
32. Mattioli TA, et al. (1991) Primary donor structure and interactions in bacterial reaction centers from FT Raman spectroscopy. *Biochemistry* 30:4648–4654.
33. Spiedel D, et al. (2002) Tuning of the optical and electrochemical properties of the primary donor bacteriochlorophylls in the reaction centre from *Rhodobacter sphaeroids*: Spectroscopy and structure. *Biochim Biophys Acta* 1554:75–93.
34. Hughes JM, Hutter MC, Reimers JR, Hush NS (2001) Modeling the bacterial photosynthetic reaction center. *J Am Chem Soc* 123:8550–8563.

35. Palaniappan V, et al. (1993) Comprehensive resonance Raman study of photosynthetic reaction centers from *Rhodobacter-sphaeroides*. *J Am Chem Soc* 115:12035–12049.
36. Yamasaki H, Takano Y, Nakamura H (2008) Theoretical investigation of the electronic asymmetry of the special pair cation radical in the photosynthetic type-II reaction center. *J Phys Chem B* 112:13923–13933.
37. Fischer MR, et al. (1992) C-13 magic-angle spinning NMR-study of the light induced and temperature-dependent changes in *Rhodobacter sphaeroides* R26 reaction centers enriched in 4′-^{13}C tyrosine. *Biochemistry* 31:11038–11049.
38. Shochat S, et al. (1995) C-13 MAS NMR evidence for a homogeneously ordered environment of tyrosine-M210 in reaction centers of *Rhodobacter sphaeroides*. *Spectrochim Acta, Part A* 51:135–144.
39. Diller A, et al. (2007) N-15 photochemically induced dynamic nuclear polarization magic-angle spinning NMR analysis of the electron donor of photosystem II. *Proc Natl Acad Sci USA* 104:12767–12771.
40. Shelnutt JA, et al. (1998) Nonplanar porphyrins and their significance in proteins. *Chem Soc Rev* 27:31–41.
41. Feher G, Okamura MY (1978) in *The Photosynthetic Bacteria*, eds Clayton RK, Sistrom WR (Plenum, New York), pp 349–386.
42. Okamura MY, Isaacson RA, Feher G (1975) Primary acceptor in bacterial photosynthesis—Obligatory role of ubiquinone in photoactive reaction centers of *Rhodopseudomonas spheroides*. *Proc Natl Acad Sci USA* 72:3491–3495.
43. Bennett AE, et al. (1995) Heteronuclear decoupling in rotating solids. *J Chem Phys* 103:6951–6958.
44. Schleyer PV, et al. (1996) Nucleus-independent chemical shifts: A simple and efficient aromaticity probe. *J Am Chem Soc* 118:6317–6318.
45. Schreckenbach G, Ziegler T (1995) Calculation of NMR shielding tensors using gauge-including atomic orbitals and modern density-functional theory. *J Phys Chem* 99:606–611.
46. Amsterdam density functional program, theoretical chemistry Version no. 2008.01″ (2008) (Vrije Universiteit, Amsterdam). Available at: http://www.Scm.Com. Accessed 17 January 2009.
47. Velde GT, et al. (2001) Chemistry with ADF. *J Comput Chem* 22:931–967.
48. Becke AD (1988) Density-functional exchange-energy approximation with correct asymptotic-behavior. *Phys Rev A At Mol Opt Phys* 38:3098–3100.
49. Perdew JP (1988) Energetics of charged metallic particles—From atom to bulk solid. *Phys Rev B Condens Matter* 37:6175–6180.
50. Grimme S (2006) Semiempirical GGA-type density functional constructed with a long-range dispersion correction. *J Comput Chem* 27:1787–1799.